Three-Dimensional Flow and Turbulence Structure in Electrostatic Precipitator

by

Thorvald Ullum[(1)], Poul S. Larsen[(2)]

Department of Mechanical Engineering, Fluid Mechanics Section

Technical University of Denmark, Building 403, DK-2800 Lyngby, Denmark

and

Oktay Özcan[(3)]

Visiting Professor, Currently at the Faculty of Aeronautics and Astronautics

Technical University of Istanbul, 80626, Istanbul, Turkey

[(1)]E-Mail: tu@mek.dtu.dk ,[(2)]E-Mail: psl@mek.dtu.dk ,[(3)]E-Mail: ozcano@atlas.cc.itu.edu.tr

ABSTRACT

Stereo PIV is employed to study the three-dimensional velocity and turbulence fields in a laboratory model of a negative corona, barbed-wire, smooth-plate, electrostatic precipitator (figure 1). The study is focused on determining the parametric effects of axial development, mean current density J_m and bulk velocity U_0 on secondary flows and turbulence levels and structures due to the action of the three-dimensional electrostatic field on the charged gas. At constant bulk velocity (U_0 = 1 m/s) and current density (J_m = 0.4 mA/m^2), secondary flows in the form of rolls of axial vorticity with swirl numbers up to S = 0.3-0.4 are found to level off after 4-5 electrodes, being most regular in the central unit cells defined by the periodic geometry of pin-electrodes. The corresponding image-mean turbulence intensity $\langle Tu \rangle$ increases to about 20% from the 1st to the 7th electrode with a consistent anisotropy of normal Reynolds stresses. The effects of U_0 and J_m on S and Tu (at fixed position between 6th and 7th electrode) are reasonably correlated by the electrohydrodynamic modulus $N_{EHD} = (J_m/b_i)l_y/(\frac{1}{2}\rho U_0^2)$, where b_i denotes the ion mobility and l_y the electrode-plate distance.

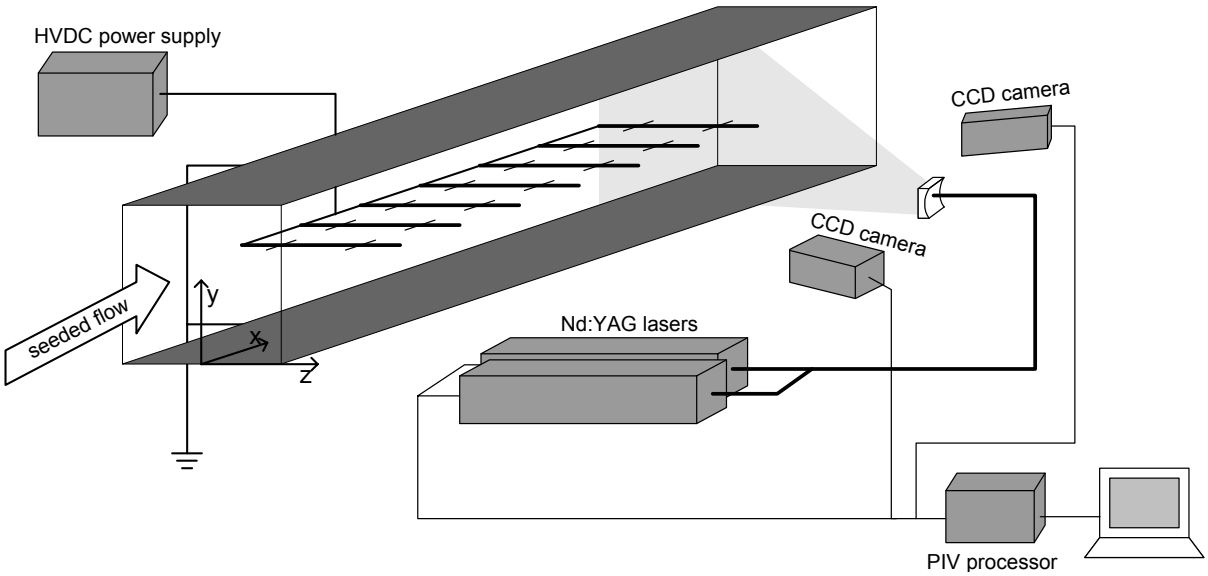

Fig. 1. The 0.2×0.2×1.0 m test section with 7 electrodes, coordinate system, and PIV setup (schematic).

1. INTRODUCTION

Although in practical use for more than half a century (Oglesby and Nichols, 1978) the quest for modeling and optimizing the industrial electrostatic precipitator (ESP) continues at different levels of detail and complexity. Relevant topics range from local physics to global design and include: modeling the corona discharge process (Peek, 1929, Anagnostopoulos and Bergeles, 2001); calculating the electric field and current distribution between discharge electrode and collector plate (Zamany, 1992, 1995, Anagnostopoulos and Bergeles, 2001), including particle charge and accumulated dust layer on collector plate (Zamany, 1992); analyzing the effect of electric field on gas flow causing secondary flows and increased turbulence (Yamamoto and Velkoff, 1981, Thomsen *et al.*, 1982, Larsen and Christensen, 1988); particle charging (McDonald, 1984), motion (Schmid, 1998), precipitation (Zamany, 1992, Parasram, 2001, Blanchard *et al.*, 2001) and possible re-entrainment resulting from rapping; modeling of overall efficiency in terms of percent of initial dust load precipitated out (Lenonard, *et al.,* 1980, Larsen and Sorensen, 1984), which includes the flow management at the inlet through screens and guide vanes (Nielsen *et al*., 2001, Agamemnon, *et al.*, 2002) to achieve a desirable overall gas distribution to the usually tall channels formed by parallel collector plates.

The present experimental study is concerned with local flows and turbulence in a negative corona, barbed-wire, smooth-plate electrostatic precipitator. Here, the non-uniform electrostatic field and the induced charge density of gas ions give rise to a complex three-dimensional, spatially periodic body force field acting on the charged gas flow (Zamany, 1992). As a result the incoming uniform bulk flow gets distorted as secondary flows develop and turbulence is generated. Such flow effects impair the efficiency of the electrostatic precipitator (Larsen and Sorensen, 1984) and it is desirable to be able to predict these effects by means of CFD-models. It is noted that for positive corona, wire-plate configurations secondary flows are two-dimensional perturbations on the bulk flow (Yamamoto and Velkoff, 1981, Leonard *et al*., 1983, Parasram, 2001), hence less detrimental to the efficiency, but in practice most installations employ negative corona. Currently, three-dimensional numerical calculations of electric fields and turbulent flows are being made (Zamany, 1992, 1995), but results on the flow and particle transport rely on proper modeling of turbulence and associated effective turbulent transport of momentum and particulate matter. In addition, the boundary conditions at collector plates need further modeling to take into account deposition fluxes and possible particle re-entrainment. It is the purpose of the present study to provide detailed experimental data to show parametric effects of electric current density and bulk flow velocity on the strength of secondary flow and turbulence and their axial development from the first electrode and downstream.

2. EXPERIMENTAL SETUP

2.1 Test section

The experimental study has been carried out in a specially designed wind tunnel with a 0.2×0.2 m by 1.0 m long test section (figure 1) placed downstream of 16:1 contraction and a 1.3 m straight section. The test section has 2 grounded aluminum sides that serve as collector plates, and 2 glass sidewalls that support up to 7 discharge electrodes, starting at x = 200 mm from the inlet, spaced 100 mm apart and connected to a low-ripple, high voltage, DC-power supply (Hypotronics, model 800PL). The type CA-100-100 pin electrodes employed in the study are 3 mm diameter brass rods pierced by 2, axially oriented, 10 mm long and 1 mm diameter pins spaced 100 mm apart (50 mm from sidewalls, see figure 1). Pins act as fix points for the negative corona discharge, hence provide a well-defined electrical field. Three 60×160 mm ports in one collector plate can be replaced by a 'checkerboard' measuring plate containing 6×16 electrically separated 1 cm^2 squares to give distributions of local current density to the collector plate (Zamany, 1995).

In practice electrodes and collector plates of an industrial electrostatic precipitator are vertical, but to facilitate optical access for PIV the model was rotated 90° so the grounded collector plates were horizontal. The effect of gravity on seeding particles is negligible since the terminal velocity of a 5 μm diameter seeding particle would be less than 1 mm/s. Figure 1 also defines the coordinate system to which data are referred, the origin being located at the midpoint of the bottom plate at the inlet to the 1.0 m long test section.

The geometry of the test section with type CA-100-100 pin electrodes suggests a spatially periodic arrangement of $l_x \times l_y \times l_z$ = 100×100×50 mm 'unit cells' when boundary effects at sidewalls are ignored, i.e. a total of 8 such unit cells across the 200×200 mm cross section (see figure 2). The small aspect ratio of pin spacing on electrodes to

channel-width was a compromise between good PIV access and unit-cell Reynolds numbers comparable to those of commercial precipitators (typically of 3-400 mm collector plate spacing).

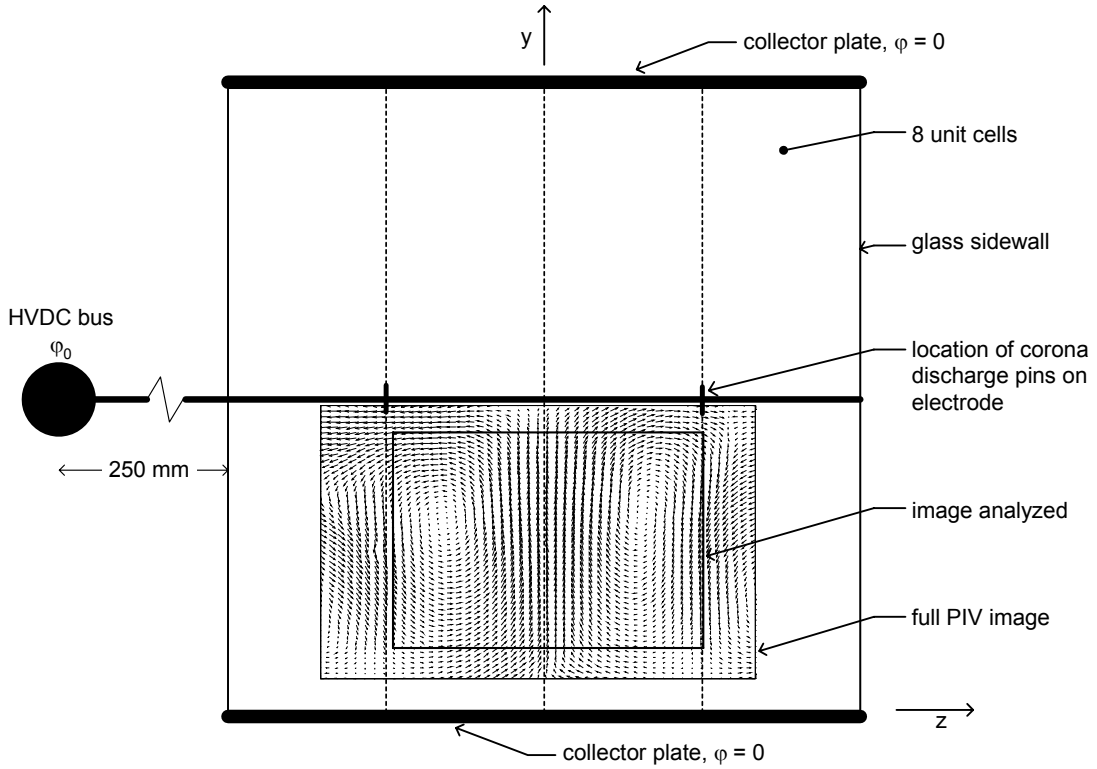

Fig. 2. Cross section of 200×200 mm test section showing the location of full PIV image and region analyzed. Dashed lines indicate symmetry of unit cells. (Discharge pins on electrodes point in axial direction in reality).

In regard to flow, unit cells at glass sidewalls are atypical because a no-slip boundary condition replaces that of symmetry found in other unit cells. But since wall boundary layers are thinned by secondary flows this effect is relatively small.

In preliminary test runs, however, the observed secondary flows driven by the electrical field proved to vary all depending on type of seeding used and frequency of cleaning the glass sidewalls for deposited seeding. Apparently the boundary condition at the glass was not one of symmetry but one of some arbitrary distribution of potential. The initial glycerol-water seeding, being electrically conducting was therefore replaced by olive oil seeding. Also, the length of electrode extensions connecting to the high-voltage bus (HVDC bus) outside the test section was increased to 250 mm in order to reduce electric field distortions causing lack of symmetry (see figure 2). These measures gave flows that were fairly reproducible and periodic according to unit cells, but since negative corona discharge is inherently unstable, even from fix points as the pins of the present electrodes, variations in time were observed. A perfectly regular cell pattern of flow structures does not appear in the data, but such variations are considered to be representative for conditions in industrial precipitators.

2.2 Instrumentation for flow and velocity fields

Bulk flow mean velocity U_0 was measured by a standard orifice-plate flow meter, the pressure drop being read from a precision micro-manometer. Voltage and total current to electrodes were read from instruments integrated into the high-voltage power supply. However, an accurate value of actual mean current density to the collector plate was calculated from measured voltage over precision resistors build into the 6×16-checkerboard plate. The total current to all electrodes, when converted into mean current density and compared to the actual local value, was used to detect any indication of current leaks along glass sidewalls.

Instrumentation for velocity and turbulence data consisted of a digital stereo PIV system (see figure1). The optical system was mounted on a three-axes traversing bench allowing selection of measuring field in the cross section of the test section as well as axial traverse. Atomized 2–5 μm diameter droplets of olive oil served as seeding. Such particles become negatively charged by the charge carrying gas and ultimately precipitate on collector plates and to some extent on glass walls and electrodes. Thus the measured particle velocity is different from the gas velocity.

A Continuum Surelite I-10 double-cavity Nd:YAG laser with a maximum output of 200 mJ per pulse of duration 4-6 ns provided input to a Dantec 80X11 high-power light-guiding arm with an 80X20 optics producing a 1.0-1.5 mm thick light sheet with a divergence angle of 15° in the y,z-plane of investigation. Two 1k×1k dual frame single exposure CCD cameras (Kodak Megaplus ES1.0) placed at viewing angles of about ±45° relative to the laser sheet, imaged the flow area $z \in$ [-67,66] mm by $y \in$ [10,99] mm, corresponding to most of the two central unit cells in the lower part of the test section. It was not possible to eliminate all reflections from deposited seeding on glass walls, particularly near electrodes, hence images of some test series lacked data at various spots. Also, it was not possible to capture the velocity field close to the collector plate, which would require use of fluorescent seeding particles. Thus the resulting analyzed area covers $z \in$ [-45,50] mm by $y \in$ [20,90] mm (see figure 2).

The pulse lasers and cameras were interfaced to a Dantec FlowMap PIV2000 processor with 2D/3D software to handle calibration for out-of-plane velocity and preliminary data reduction, which employed adaptive correlation on 32×32 pixel interrogation areas with a 50% overlap, yielding the three components of 49×52 instantaneous velocity vectors. The timing between two light pulses was limited by the large out-of-plane velocity and was in the range 130-200 μs. All subsequent processing was done in Matlab.

The experimental accuracy of bulk flow was about ±2%, of mean current density ±0.02 mA/m^2, of voltage ±0.05 kV, and (for one vector map sample) ±0.08 m/s for in-plane and out-of-plane components. The latter estimates are based on an accuracy of particle displacement of about 0.1 pixels. With a sample size of $N_s = 200$ and, say a mean velocity of 0.5 m/s and turbulence intensity of 15%, the relative uncertainty would be of the order of 1% on mean velocity and 7% on rms-velocity (Ullum *et al.*, 1998).

2.3 Particle drift and electrostatic field

A small seeding particle of diameter d_p having electric charge q in an electric field of strength $\boldsymbol{E}$ attains a terminal electric drift velocity relative the surrounding gas determined from the balance of Stokesian drag with Coulomb force, yielding $\boldsymbol{V}_e = q\boldsymbol{E}/(3\pi\mu\, d_p) \equiv b_p\boldsymbol{E}$, where $b_p = q/(3\pi\mu\, d_p)$ denotes the mobility of the particle. The charge depends on the diameter of the particle and based on experiments (McDonald *et al.*, 1980) the mobility may be expressed as $b_p \approx 6.8\times10^{-3}\, d_p^{0.75}$ m^2/Vs for fully charged spherical particles in air at room temperature. Since the time constant $\tau_p = d_p^2\rho_p/18\mu$ for a $d_p = 5$ μm particle is typically of the order of 10^{-4} s, where ρ_p denotes particle density and μ the dynamic viscosity of the gas, the drift velocity is attained practically instantaneously. Thus it may be assumed that the measured particle velocity equals the sum of local gas velocity and electric drift velocity, $\boldsymbol{V}_p = \boldsymbol{V} + \boldsymbol{V}_e$. Hence computed values of the steady three-dimensional electric drift velocity was subtracted from the measured particle velocity to give the gas velocity.

The electrostatic field in a unit cell between discharge electrode and collector plate is governed by the Maxwell equations and charge conservation, which reduce to

$$\nabla.\boldsymbol{E} = \rho_i/\varepsilon_0 \; ; \qquad \nabla.\boldsymbol{J} = 0 \; , \tag{1}$$

where $\boldsymbol{E} = -\nabla\varphi$ is the field strength, φ the potential, ρ_i the charge density of gas ions (ignoring the small contribution of charge on seeding particles and free electrons), ε_0 the electric permittivity, and $\boldsymbol{J}$ the current density. Ignoring the convective current, which is negligible for the prevailing small gas velocities, the current density is given by the Ohm law, $\boldsymbol{J} = \rho_i\, b_i\, \boldsymbol{E}$, where b_i denotes the mobility of gas ions (= 2.1×10^{-4} m^2/Vs for air at room temperature, Zamany, 1992). The nonlinear numerical problem then consists of solving for distributions of both the potential φ and the charge density ρ_i for a unit cell from

$$\nabla^2\varphi = -\rho_i/\varepsilon_0 \; ; \qquad \boldsymbol{E}.\nabla\rho_i - \rho_i^2/\varepsilon_0 = 0 \, , \tag{2}$$

subject to boundary conditions: $\partial/\partial n = 0$ at symmetry planes, $\varphi = 0$ at the collector plate, $\varphi = \varphi_0$ at the electrode, and $\rho = \rho_0$ at corona points, which is adjusted iteratively until the calculated mean current density J_m at the collector plate equals that measured experimentally for the specified electrode potential φ_0 . Given the potential distribution, the Coulomb force acting on the gas can be calculated from $\boldsymbol{F}_e = \rho_i \boldsymbol{E}$, and the drift velocity of seeding particles from $\boldsymbol{V}_e = b_p \boldsymbol{E}$.

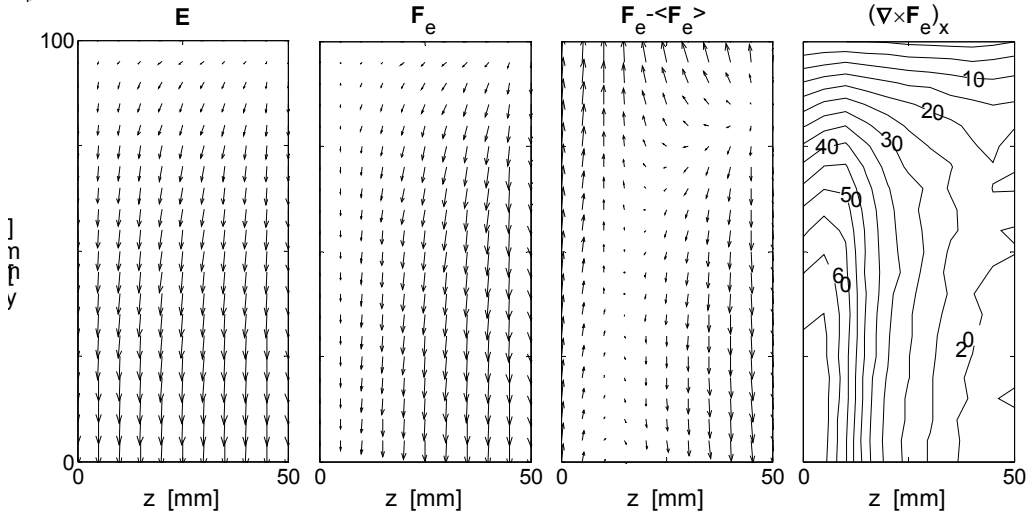

Fig. 3. Calculated electrostatic field in y,z-plane of unit cell mid between 2 electrodes; pins with corona discharge in upper right corner. From left to right: electrical field $\boldsymbol{E}$*, Coulomb force* $\boldsymbol{F}_e = \rho_i \boldsymbol{E}$ *acting on gas, its departure from the mean, and its curl (vorticity source, contour values in* N/m^4*).*

Figure 3 shows the solution of field calculations from (2) for $J_m = 0.4$ mA/m^2 in terms of the $\boldsymbol{E}$-field (which is proportional to $\boldsymbol{V}_e$) in the *y*,*z* symmetry plane between two electrodes, the Coulomb body force $\boldsymbol{F}_e = \rho_i \boldsymbol{E}$ acting on the gas, its departure from the cell-mean $\boldsymbol{F}_e - \langle \boldsymbol{F}_e \rangle$, and its curl, which in this plane has only the axial component $\Omega_x = (\nabla \times \boldsymbol{F}_e)_x$. The cell-mean body force merely causes a pressure stratification while the departure from the mean will tend to drive a secondary flow in the form of axial rolls superposed the axial bulk flow (see figure 2). This may also be viewed as a result of the axial vorticity source distribution. Upstream and downstream of the symmetry plane shown, the electric force field is three-dimensional but with components in *y*,*z*-planes having similar features in terms of sign, hence contributing to drive the axial rolls. As long as the inertia of axial bulk flow is large (N_{EHD} small) axial components of the electric force field, found particularly near electrodes, will give only small perturbations on the flow.

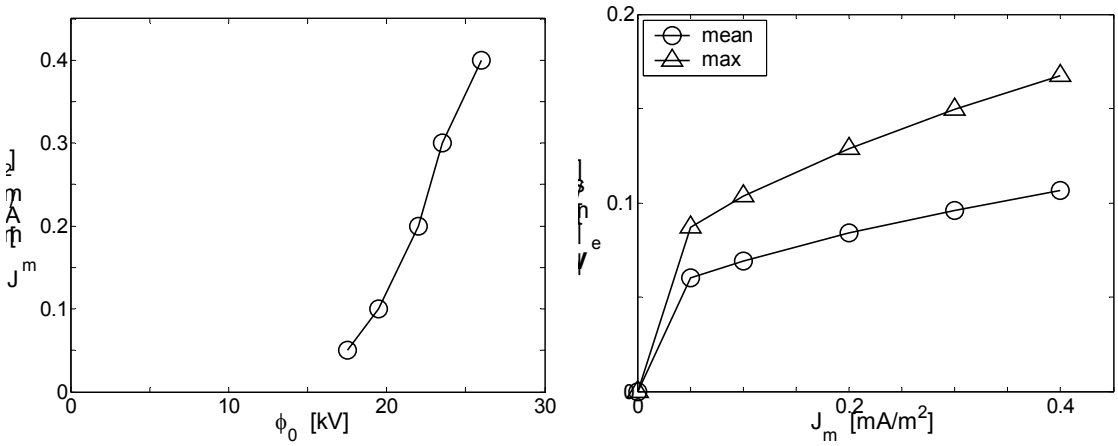

Fig. 4. Measured current density versus applied voltage (left) and calculated particle drift velocity for a $d_p = 5$ *μm particle as function of current density (right). Mean and maximum values for drift velocity are calculated in the mid plane between two electrodes.*

Figure 4 shows the current-voltage characteristic in terms of mean current density J_m versus electrode potential φ_0, recorded in the region near 5th–7th electrode for 7 CA-100-100 electrodes, indicating corona ignition at about 15 kV.

The computed magnitude of electric drift velocity $|\boldsymbol{V}_e|$ of 5 μm diameter seeding droplets is illustrated in figure 4 in terms of cell-max and cell-mean values as function of J_m. In some areas the correction of the measured particle velocities is as high as 20%, and even higher values are found near pin-electrodes and near the collector plate. Near the collector plate the electric drift is dominating being perpendicular to the gas velocity that vanishes in the boundary layer.

2.4 Data analysis

Image records of size N_s for a given test were processed for the usual statistical mean values of velocity components U, V, W and Reynolds stresses $\overline{uu}$, $\overline{vv}$, $\overline{ww}$, $\overline{uv}$, $\overline{vw}$, $\overline{wu}$. As a measure of the bulk turbulence level Tu we use the isotropic part of the Reynolds stress tensor normalized with the mean bulk velocity U_0, and we also examine the normalized deviator stresses denoted a_{ij},

$$Tu = (\overline{u_k u_k}\,/3)^{1/2}/U_0 \;; \qquad k = \tfrac{1}{2}\,\overline{u_k u_k}\;; \qquad a_{ij} = \overline{u_i u_j}\,/\,k - 2/3\,\delta_{ij}, \tag{3}$$

where k denotes the turbulent kinetic energy. In addition to point-values of variables in the image field, also spatial image-mean and cell-mean values of variables, computed by simple averaging over the area in question, are found to be useful to illustrate general trends.

Distributions of axial vorticity ω_x of the mean velocity field in the image plane are calculated from the circulation along the boundary of 4 cells surrounding a given point using the Stokes theorem.

The secondary flow in the y,z-plane may be characterized by a swirl number, S, the ratio of angular momentum flow to axial momentum flow over the area of a unit cell of hydraulic radius L = 2×Area/Perimeter,

$$S = G_\theta/(LG_x) \;; \quad G_\theta = \int_A \rho U(\boldsymbol{r}\times\boldsymbol{V})_x \,\mathrm{d}A \;; \quad G_x = \int_A \rho UU \,\mathrm{d}A \;, \tag{4}$$

where contributions from pressure and turbulent velocity fluctuations have been ignored. The angular momentum is computed with respect to the point of maximum absolute vorticity $|\omega_x|$ determined from contour plots of ω_x (see figure 6 below). In the processing of data, the positive and negative sign of ω_x, respectively, determine the area considered in calculating the swirl number for the positive and negative roll in the image.

3. RESULTS

The experimental results presented in this section cover 3 test series characterized by axial location x of y,z-plane, bulk velocity U_0, and mean current density J_m, as summarized in Table 1. All tests are for 7 CA-100-100 electrodes. The sample sizes of image records used for processing the presented data are N_s = 200-400.

Table 1. Test series

Test series	x (mm)	U_0 (m/s)	J_m (mA/m^2)
1	750	1.0	0, 0.05, 0.1, 0.2, 0.3, 0.4
2	750	1.0, 1.15, 1.41, 2.0	0.4
3	250, 350, 450, 550, 650, 750	1.0	0.4

Dimensional analysis suggests two dimensionless groups for the dynamics of the flow, the Reynolds number and the electro-hydrodynamic modulus

$$\mathrm{Re} = U_0\, l_y/\nu \;; \qquad \mathrm{N_{EHD}} = (J_m/b_i)\, l_y / (\tfrac{1}{2}\,\rho\, U_0^2) \;, \tag{5}$$

being respectively the ratio of inertia to viscous forces and the ratio of transverse electric force to axial flow inertia, similar to an inverse Froude modulus. The mean electric force on the gas in the considered symmetry planes is derived by combining the Coulomb force with the Ohm law as $< F_{e,\,y} > = < \rho_i E_y > = < J_y/b_i > = J_m/b_i$, and the characteristic length is the distance from electrodes to collector plate. In addition to the dynamic groups there are geometric groups associated with the electrode form and the unit cell. The effect of the latter on strength of secondary flows has been studied previously (Larsen and Christensen, 1988).

3.1 Velocity and turbulence fields

The *V*,*W*-velocity vector plot in the full PIV image in figure 2 shows the general features of the secondary gas flow, $\boldsymbol{V} = \boldsymbol{V}_p - \boldsymbol{V}_e$, driven by the electric field, the flow being directed towards the collector plate in the *x*,*y*-planes of pins on electrodes and returning in between (case of $x = 750$ mm, $U_0 = 1.0$ m/s, $J_m = 0.3$ mA/m^2). The figure shows two axial rolls of opposite sign and approximately same strength located at the two central unit cells in the lower half of the test section. The velocity field visible outside these cells suggests the existence of distorted rolls in the two cells near the sidewalls.

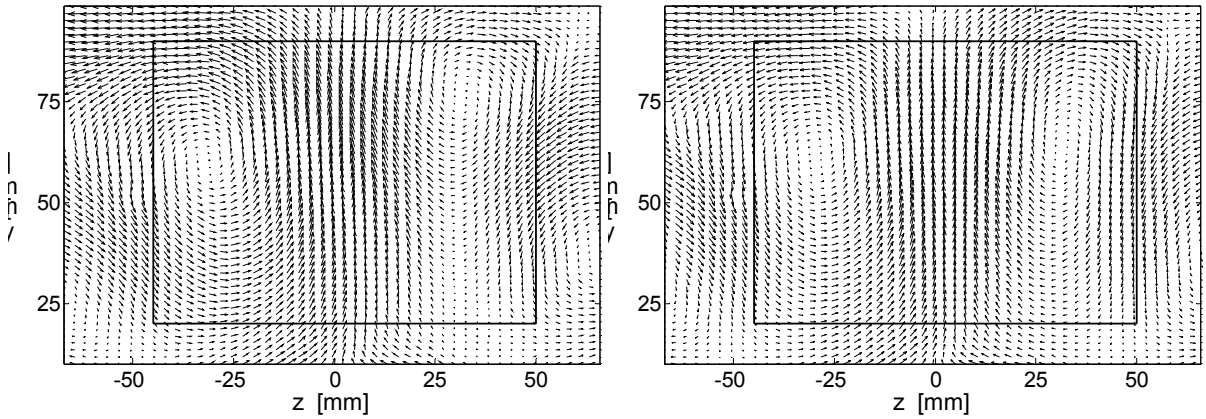

Fig. 5. Measured in-plane velocity field (W,V) for $J_m = 0.4$ mA/m^2 (left), $J_m = 0.3$ mA/m^2 (right). $x = 750$ mm, $U_0 = 1.0$ m/s.

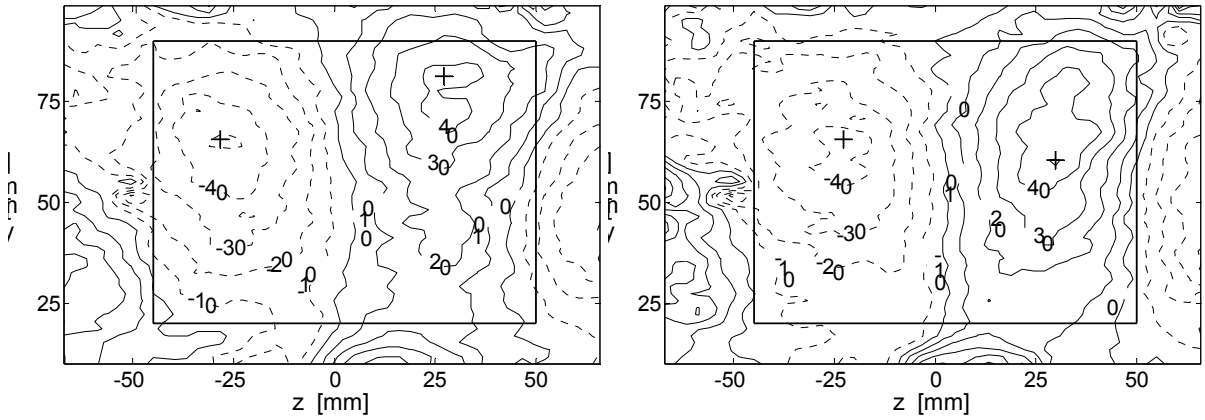

Fig. 6. Calculated axial vorticity ω_x based on velocity fields in Fig. 5. (+) denotes locations of maximum and minimum values. Contour levels in s^{-1}.

To illustrate the typical irregularities of the resulting secondary flows observed, figure 5 shows *V*,*W*-velocity vector plots in the full PIV image for two values of current density, $J_m = 0.4$ and 0.3 mA/m^2, both at $x = 750$ mm, $U_0 = 1.0$ m/s. Figure 6 shows the corresponding vorticity fields in which the max values of absolute ω_x are marked (+) in each unit cell. Again, such variations must be considered to be typical and realistic for an actual electrostatic precipitator, and they contribute to the scatter in the data presented.

Figure 7 presents a comparison between experimental data for a downstream unit cell at the reference case (x = 750 mm, U_0 = 1.0 m/s, J_m = 0.4 mA/m^2) and corresponding results from preliminary Large Eddy Simulations (LES). The figure shows (from left to right) a vector plot of secondary flow V,W, contours of axial velocity U/U_0, turbulence levels Tu, and contours of axial vorticity ω_x. The LES calculations were made by the finite difference code PEGASE, developed at ONERA (Lê et al., 1997), and employed the Mixed Scale subgrid scale model in combination with a selective function (Lenormand, et al., 2000). The computational cubic domain represents 0.2 m of the experimental test section containing 2 electrodes in 16 unit cells and a spatial resolution of 65×65×81 nodes. The boundary conditions are periodic in x and z and the no slip condition is imposed in y. The periodicity in x corresponds to the fully developed problem, hence the thinning of the wall boundary layers at the lower collector plate due to secondary flow is clearly visible. As expected, LES results are considerably more regular than PIV data, however, the levels of Tu and ω_x show satisfactory agreement. The maximum in-plane velocity is 0.64 m/s and 0.38 m/s for PIV and LES respectively and hence deviates more than the other variables shown in Figure 7.

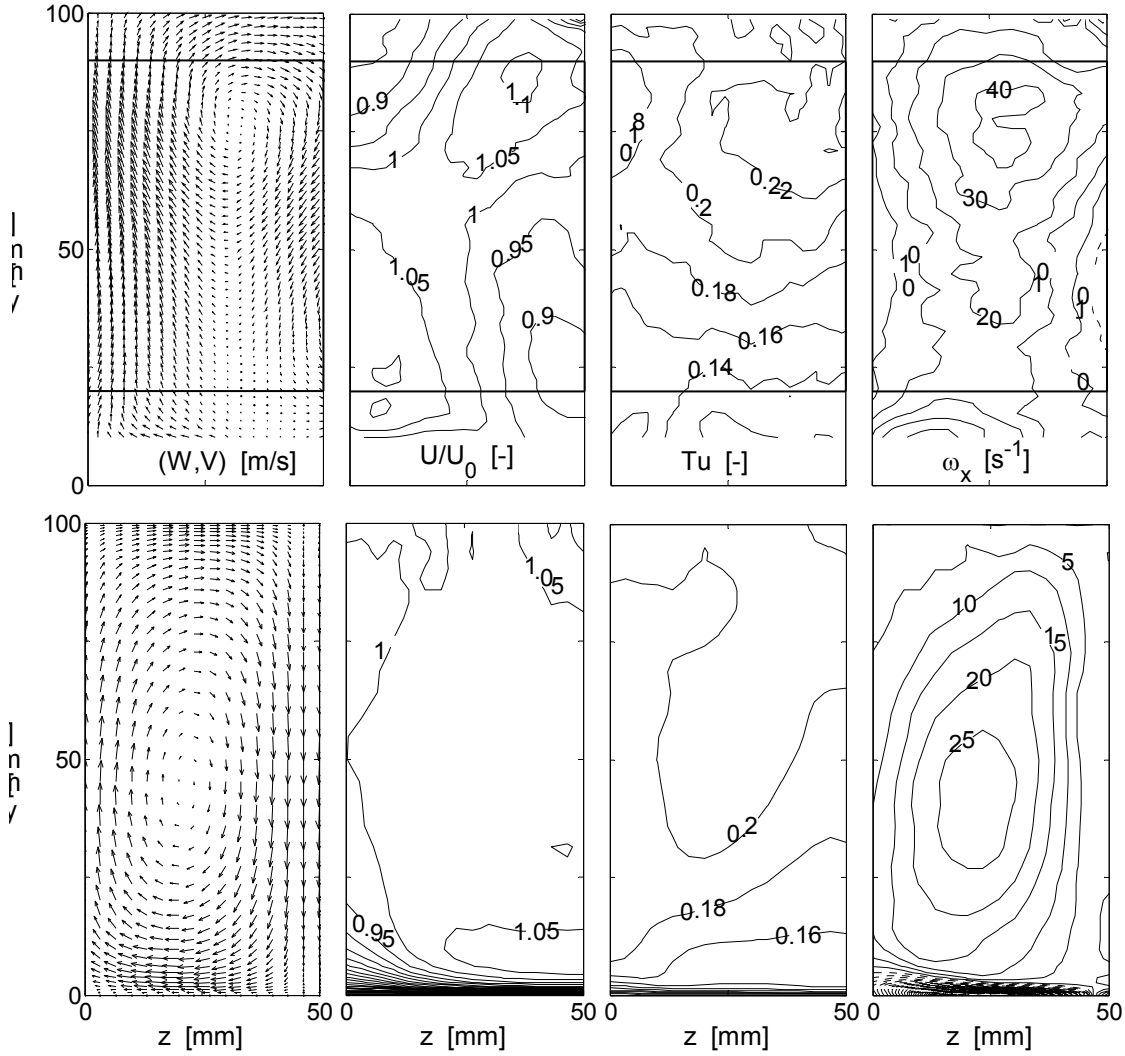

Fig. 7. Comparison between PIV data (top row) and LES data (bottom row). From left to right: In-plane secondary flow (W,V); axial velocity U/U_0; turbulence intensity Tu; axial vorticity ω_x. (x = 750 mm, U_0 = 1.0 m/s, J_m = 0.4 mA/m^2).

3.2 Flow development and parametric effects

Figure 8 shows the axial development of the counter-rotating rolls appearing in the two unit cells of the image, the strength being measured by the swirl number S of (4), and the image-mean turbulence intensity <Tu> of (3), both

for test series 3. While S appears to level off at a value of about $|S| \approx 0.3\text{-}0.4$, $\langle Tu \rangle$ continues to increase nearly linearly with distance from $x = 250$ mm, approaching nearly 20% at $x = 750$ mm. The fairly high reference value at zero current of about 8% at the downstream position $x = 750$ mm is a result of wakes from electrodes as well as some boundary layer effects. The asymmetry of the two rolls is clearly expressed by their different swirl numbers, the left roll being roughly 20% stronger than the right roll, downstream of $x = 450$ mm.

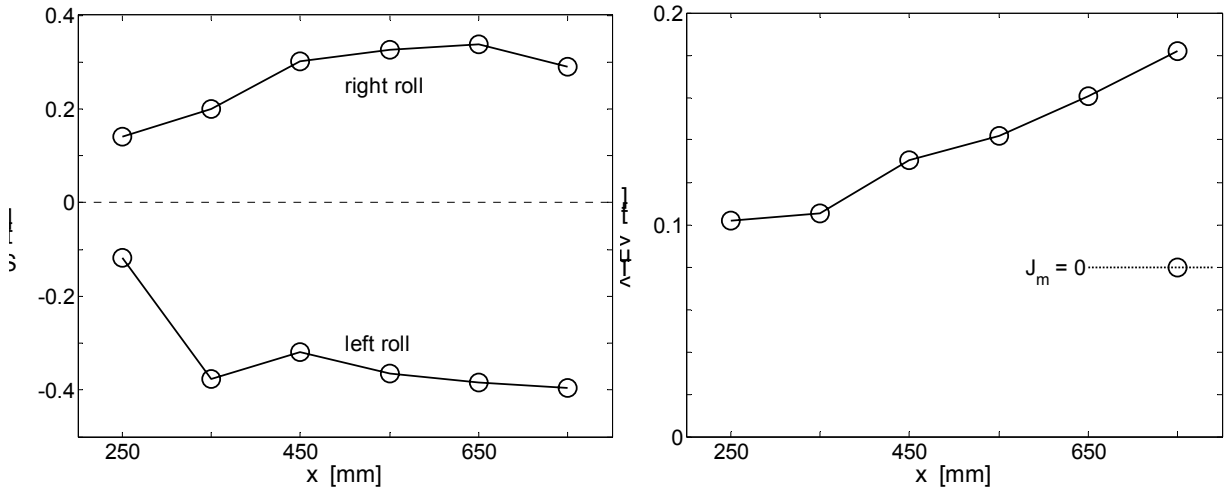

Fig. 8. Axial development of image-mean swirl number for the two rolls (left) and mean turbulence intensity <Tu> (right). Reference <Tu>-level at $J_m = 0$. Test series 3 ($U_0 = 1.0$ m/s, $J_m = 0.4$ mA/m^2).

Figure 9 shows the parametric effect of both bulk velocity and current density from test series 1 and 2 on swirl number and turbulence intensity at one axial position ($x = 750$ mm) by using $N_{EHD} = (J_m/b_i)\, l_y / (\tfrac{1}{2}\rho U_0^2)$ of (4) to combine the effects. The increase in S and $\langle Tu \rangle$ with N_{EHD} and asymmetry effects are similar to those of axial development in figure 8, roll strengths leveling off while turbulence intensity appears to continue to increase. The fairly good correlation of the data by N_{EHD} confirms that the magnitude of parameters S and $\langle Tu \rangle$ is a bulk flow phenomenon.

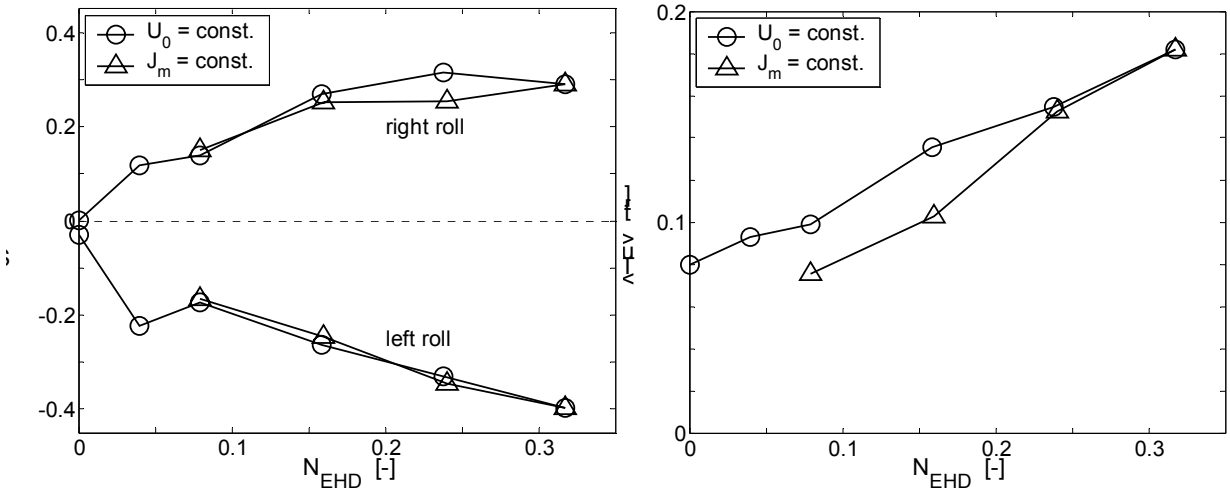

Fig. 9. Image-mean swirl number for the two rolls (left) and mean turbulence intensity (right) as function of $N_{EHD} = (J_m/b_i)\, l_y / (\tfrac{1}{2}\, \rho\, U_0^2)$, combining the effects of changing current density J_m and bulk velocity U_0. Test series 1 and 2 ($x = 750$ mm).

3.3 Reynolds stresses

The data reveals a consistent and significant anisotropy of normal Reynolds stresses with $\overline{ww} > \overline{uu} > \overline{vv}$, as shown in figures 10 and 11 in terms of image-mean values. Figure 10 shows the effect of axial development (test series 3). Figure 11 shows the effect of current density (test series 1) and the effect of bulk velocity (test series 2), both presented as function of N_{EHD}, which for these variables does not seem to correlate the two parametric effects well, particularly not for $N_{EHD} < 0.15$. It is noted that the anisotropy is as large as about $\overline{ww} / \overline{vv} \approx 2$.

The data for distributions and cell-mean values of the components of the normalized deviatoric Reynolds stress a_{ij} of (3) have been examined. Results show that a_{33} is always positive and in absolute magnitude generally larger than the two other normal components, being generally negative with a_{11} smallest. The shear components of a_{ij} are all small, a_{23} being positive and the largest of the three. It may be concluded that the turbulence generated by the electric field is a highly anisotropic bulk turbulence with small or negligible shear effects.

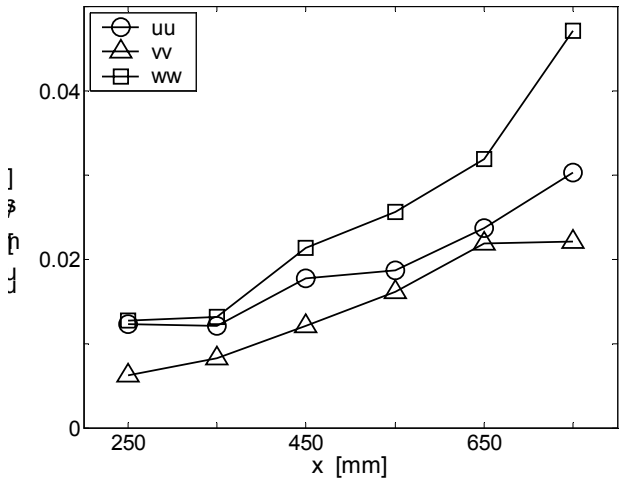

Fig. 10. Anisotropy of normal Reynolds stresses. Test series 3: effect of axial development.

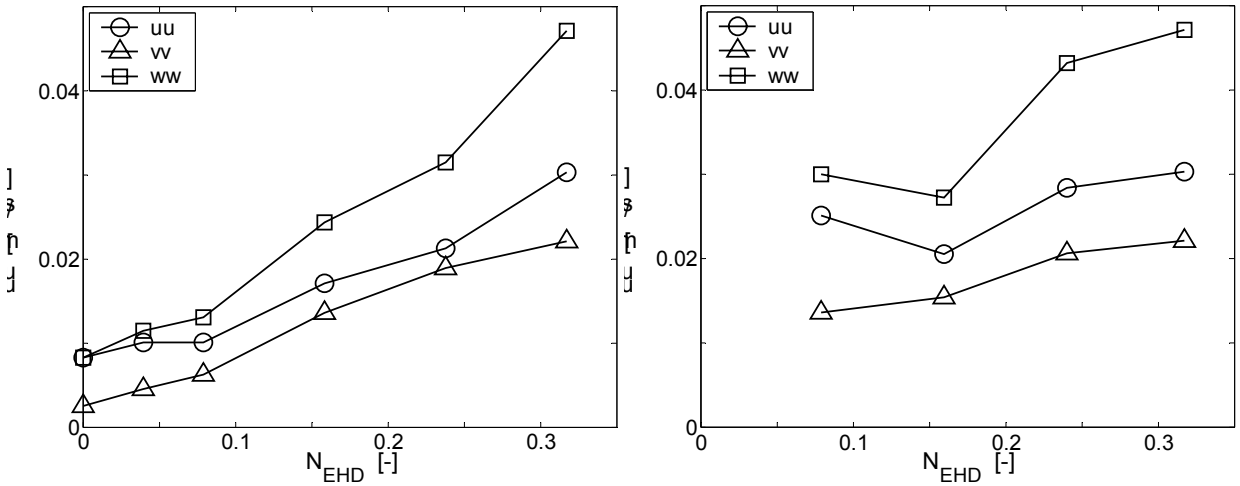

Fig. 11. Anisotropy of normal Reynolds stresses. Test series 1: effect of current density (left); test series 2: effect of bulk velocity (right).

4. CONCLUSIONS

The present experimental study, employing the stereo PIV technique, has provided a large amount of data on the three-dimensional velocity field in a laboratory model of a negative corona, barbed-wire, smooth-plate electrostatic precipitator. The study has focused on parametric effects of axial development, mean current density J_m and bulk velocity U_0 on secondary flows and turbulence levels due to the action of the three-dimensional electrostatic field on the charged gas. Due to the geometry of 200×200 mm test section and the present type CA-100-100 barbed-wire electrodes, 8 'unit cells' of cross section 50×100 mm with symmetric and antisymmetric electrostatic fields and resulting secondary flows were expected. Most data are therefore presented for one 'unit cell'. Also, to obtain the gas velocity, the measured velocities of seeding particles are subtracted computed values of electric drift velocity. Any additional contributions to the rms-velocity from variation in electric drift velocity with particle diameter for a size distribution of seeding particles is considered to be negligible and is ignored.

Data on the axial development (at J_m = 0.4 mA/m^2 and U_0 = 1.0 m/s) covered axial positions from x = 250 mm (between 1st and 2nd electrodes) to x = 750 mm (between 6th and 7th electrodes). Results show that secondary flows in the form of rolls of axial vorticity develop and reach a nearly constant level after the 5th electrode (x ≈ 600 mm), and may be characterized by a swirl number of the order of $|S| \approx 0.3$-0.4. Bulk turbulence levels increased linearly with x, showing no sign of leveling off.

Similar trends are observed when the current density J_m is increased from zero to 0.4 mA/m^2 (at constant bulk velocity U_0 = 1.0 m/s), and when the bulk velocity U_0 is decreased (at constant current density J_m = 0.4 mA/m^2). These parametric effects are combined in the electrohydrodynamic modulus, $N_{EHD} = (J_m/b_i)l_y/(\frac{1}{2}\rho U_0^2)$, being the ratio of transversal electrical force to axial bulk flow inertia, a parameter that proves to correlate the data reasonably well. These observations, as well as those derived from the Reynolds stresses suggest that the phenomena are bulk flow related. The curl of the electric body force acting on the charged gas represents a complex, three-dimensional vorticity source.

ACKNOWLEDGEMENTS

The study was funded in part by the Danish Energy Agency program EFP-2000. Advice on LES simulations by Dr. Sagaut of ONERA and constructive discussions with Dr.s L. Lind and N. F. Finderup of F.L.S.miljø a/s are acknowledged.

REFERENCES

Agamemnon, A., Anagnostopoulos, J. and Bergeles, G.C. (2002). "Prediction of the cleaning efficiency of an electrostatic precipitator", J. Electrostatics 55, pp. 111-133

Anagnostopoulos, J. and Bergeles, G. (2001). "Corona discharge simulation in wire-duct electrostatic precipitator", J. Electrostatics, 54, pp. 129-147

Blanchard, D., Dumitran, L.M. and Atten, P. (2001). Electroaerodynamic secondary flow in an electrostatic precipitator and its influence on transport of small diameter particles", Proc. 8th Intl. Conf. on Electrostatic Precipitation, May 14-17, 2001

Larsen, P.S. and Sorensen, S.K. (1984). "Effect of secondary flows and turbulence on electrostatic precipitator efficiency", Atm. Environment, 18, pp. 1963-1967

Larsen, P.S. and Christensen, E.M. (1988). "Secondary flow and turbulence in electrostatic precipitator", Laser Anemometry in Fluid Mechanics, 3, pp. 361-374, Ladoan - Instituto Superior Tecnico, 1096 Lisbon Codex, Portugal

Lê, T.H., Troff, B. Sagaut, P., Dang-Tran, K. and Phuoc, L.T. (1997). PEGASE: A Navier-Stokes solver for direct numerical simulation of incompressible flows", Intl. J. Numer. Meth. in Fluids, 24, pp. 833-861

Lenormand, E., Sagaut, P., Ta Phuoc and L. Comte, P (2000). “Subgrid-scale models for Large-Eddy Simulations of compressible wall bounded flows”, AIAA J., 38, pp. 1340-1350

Leonard, G., Mitchner, M. and Self, S.A. (1980). “Particle transport in electrostatic precipitators”, Atm. Environment, 14, pp. 1289-1299

Leonard, G., Mitchner, M. and Self, S.A. (1983). “An experimental study of the electrohydrodynamic flow in electrostatic precipitators”, J. Fluid Mech.., 127, pp. 123-140

McDonald, J.R. (1984). “Mathematical model of electrostatic precipitation”, Southern Research Institute, PB84-21267, NTIS

McDonald, J.R., Ogerson, M.H.and Mosley, R.B. (1980). “Charge measurements on individual particles exiting laboratory precipitators with positive and negative coronas at various temperatures”, J. Appl. Phys., 51, pp. 3632-3643

Nielsen, N.F., Lind, L., Akoh, E. and Hvid, S.L. (2001). “Numerical modeling of gas distribution in electrostatic precipitators, 8th Intl. Conf. on Electrostatic Precipitation, May 14-17, 2001, Birmingham, Alabama, USA

Oglesby, Jr., S. and Nichols, G.B. (1978). Electrostatic Precipitation, Marcel Dekker, Inc. New York

Parasram, N.R. (2001). “Particle Motion in Electrostatic Precipitators”, Ph.D. Dissertation, Imperial College, London, Jan. 2001

Peek, F.W. (1929)., Dielectric Phenomena in High voltage Engineering, (3rd Ed.), McGraw-Hill, New York

Schmid, H-J. (1998). “Zum Partikeltransport in Electrischen Abschneidern”. Dr.-ing. Dissertation, Facultät für Chemieingenieurswesen, TH Karlsruhe.

Thomsen, H.P., Larsen, P.S., Christensen, E.M. and Christiansen, J.V. (1982). “Velocity and turbulence fields in negative corona wire-plate precipitator”. Fourth Symp. on the Transfer and Utilization of Particulate Control Technology, Houston, Texas, 1982 (II, p.243, EPA-600/9-025 b, Nov.1984).

Ullum,U., Schmidt, J.J., Larsen, P.S. and McCluskey, D.R. (1998). "Statistical analysis and accuracy of PIV data", J. Visualization, 1, pp. 85-97

Yamamoto, T. and Velkoff, H.R. (1981). “Electrohydrodynamics in an electrostatic precipitator”, J.Fluid Mech., 108, pp. 1-18

Zamany, J. (1992). “Modeling of Particle Transport in Commercial Electrostatic Precipitators”, Ph.D. Dissertation, Danish Academy of Technical Sciences and Techn. Univ. of Denmark, Sept. 1992

Zamany, J. (1995). “Numerical modeling of electrodynamic conditions influenced by particle space charge and resistivity in electrostatic precipitators of complex geometry for industrial applications”, Inst. Phys. Conf. Ser. No. 143, pp. 357-362